Supporting Information

Pinot et al. 10.1073/pnas.1121583109

SI Text

SI Materials and Methods. ***Reagents.*** Modified *Xenopus* laevis cytostatic-factor-arrested (CSF) egg extracts, which corresponds to active cytoplasm of oocytes arrested in metaphase II of meiosis, were prepared as previously described (1–3), with one modification: The protocol was performed in absence of cytochalasin D.

Alexa-488 Phalloidin was purchased from Invitrogen (Carlsbad, Calif.). The 1,2-diacyl-sn-glycero-3-phosphocholine (egg PC), nocodazole, cycloheximide, cytochalasin D, mineral oil, Dithiothreitol, Dimethylsulfoxide, Na orthovanadate, Y-27632, ML-7, and blebbistatin were purchased from Sigma-Aldrich (St. Louis, MO).

Poly(12-hydroxystearic acid) (PHS) and poly(ethylene oxide) (PEO-30) are commercially available (Arlacel P135) and were purchased from UNIQEMA.

Recombinant Scar-WA proteins were produce as previously described (4).

Extract-in-Oil Droplet Formations. Extract-in-oil droplet formation was prepared as previously described (1, 5). Briefly, egg PC or the block-polymer PHS-PEO-PHS were first dissolved in mineral oil (0.7 mg/mL and 0.25 mg/mL, respectively). The *Xenopus* CSF egg extracts were added to the mixture of mineral oil/polymer (1% (v CSF/v oil)) at 4 °C. The mixture was gently sheared, by pipeting up and down the solution during few seconds, to generate extract-in-oil droplets. The mechanical dispersion of the biphasic solution formed micrometer-sized extract-in-oil droplets within few seconds. Immediately after this process, the mixture was incubated at 18 °C in homemade cell chambers for observations. Observation chambers were constructed by sealing an O-ring made of Polydimethylsiloxane (Sylgard, The Dow Chemical Co.) to a #1.5 clean glass coverslip [VWR International, LLC)]. Observations performed in presence or absence of nocodozole gave the same results.

Interphase Extracts. CSF extracts are cycled through interphase by addition of calcium. This causes a transient increase in Ca^{2+} that mimics fertilization. $CaCl_2$ was added to metaphase CSF extracts to a final concentration of 0.4 mM (2, 3), and the extract was incubated at room temperature for 30 min. We added 2 μg/mL cycloheximide to the extract to prevent re-entry into mitosis by avoiding Cyclin B synthesis. Experiments were performed in a temperature-controlled room of 18 °C.

Imaging. Fluorescence imaging of actin droplets was performed using an IX81 inverted microscope (Olympus) and an X60 (Plan Apo, NA 1.42) objective, equipped with an EM-CCD camera (C9102 or ImagEM, Hamamatsu Corp., Sewickley, PA). Microscope settings and functions were controlled using SimplePCI software (Hamamatsu). Image analysis was performed using ImageJ (Scion Image), SimplePCI, and MATLAB software programs.

Image Analysis and Tracking. In the field of image analysis, there are several methods to estimate motion between images. A well-known method is based on feature/interest point tracking. To track features, we need usually to consider two important steps: The first step consists in detecting the location of features in the first image; the second step amounts to computing the temporal trajectories of detected features. Among the temporal tracking methods, one of the most-known methods is the Lucas-Kanade feature tracking algorithm (6–8). The principle of the KLT algorithm is based on conventional optical flow techniques applied to a small number of features detected in the first image of the sequence. In the first step, the goal is to detect the relevant pixels. At each pixel, we consider a 2×2 local intensity variation matrix. A pixel is selected if both the eigenvalues of this 2×2 gradient matrix are larger than some threshold. The number of pixels is specified by the user, and the candidate pixels are first ranked according to the eigenvalues to determine the list of N pixels to be tracked. In the second step, the KLT algorithm defines a dissimilarity measure that quantifies the change of appearance of a pixel between the first and the second image. In our approach, we have considered a pure translational model of motion to track a given pixel through the sequence. Photobleaching artifacts are also automatically corrected during matching, and the spatial distribution of the tracked pixels is assumed relatively regular because we impose a minimum distance between selected pixels in the first image. More formally, let us consider an image pair (u, v). A pixel (or feature) $\mathbf{x}$ in the image u moves to pixel $\mathbf{x}+\mathbf{d}$ in the second image v : $v(\mathbf{x}+\mathbf{d}) = u(\mathbf{x})$. The goal is to find the location $\mathbf{x}+\mathbf{d}$ in the second image, such that $u(\mathbf{x})$ and $v(\mathbf{x}+\mathbf{d})$ are similar. To estimate the vector $\mathbf{d} = (dx, dy)$, we consider a small window W centered at pixel $\mathbf{x}$. Then, the image velocity $\mathbf{d}$ is the vector that best minimizes the dissimilarity: $E(\mathbf{d}) = \int_W (v(\mathbf{x}+\mathbf{d}) - u(\mathbf{x}))^2 w(\mathbf{x}) d\mathbf{x}$ where $w(\mathbf{x})$ is a spatial weighted function (e.g., 2D Gaussian-like function) that favors the pixels in the central area of the window W. To minimize the dissimilarity, we differentiate $E(\mathbf{d})$ with respect to the displacement vector $\mathbf{d}$ and set the result to zero. In implementation, the displacement between the pixel $\mathbf{x}$ and its estimated position is iteratively computed by using an iterative Newton-Raphson minimization procedure. Smoothing, multiresolution, and incremental techniques are recommended to improve and to speed up convergence. The predicted location of the pixel is evaluated at each frame, and the track is automatically stopped if the intensity contrast is lower than a given threshold. This computing procedure is applied independently to each pixel detected in the first step.

1. Pinot M, et al. (2009) Effects of confinement on the self-organization of microtubules and motors. *Curr Biol* 19:954–960.
2. Murray AW (1991) Cell cycle extracts. *Methods Cell Biol* 36:581–605.
3. Gaetz J, Gueroui Z, Libchaber A, Kapoor TM (2006) Examining how the spatial organization of chromatin signals influences metaphase spindle assembly. *Nat Cell Biol* 8:924–932.
4. Machesky LM, et al. (1999) Scar, a WASp-related protein, activates nucleation of actin filaments by the Arp2/3 complex. *Proc Natl Acad Sci USA* 96:3739–3744.
5. Jimenez AM, et al. (2011) Towards high throughput production of artificial egg oocytes using microfluidics. *Lab Chip* 11:429–434.
6. Lucas BD, Kanade T (1981) An iterative image registration technique with an application to stereo vision. *International Joint Conference on Artificial Intelligence* 674–679.
7. Tomasi C, Kanade T. (1991) Detection and tracking of point features. *Carnegie Mellon University Technical Report CMU-CS-91–132*.
8. Shi J, Tomasi C. (1994) Good features to track. *IEEE Conference on Computer Vision and Pattern Recognition*, (Seattle, Washington), pp 593–600.

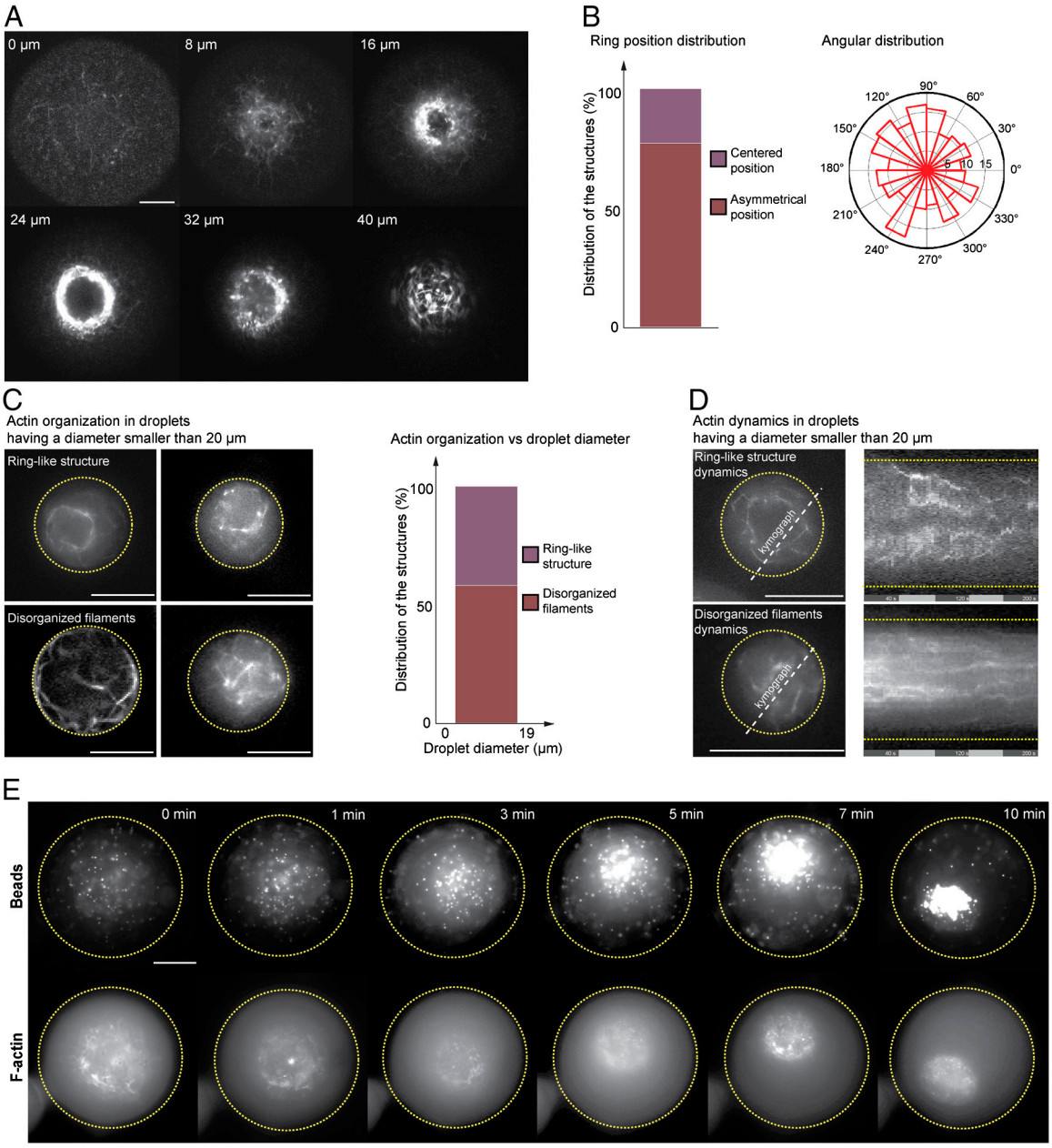

Fig. S1. (*A*) Confocal Z-scan of an actin ring-like structure within a 50 µm-diameter droplet. (*B*) Quantification of the positions of the center of the ring-like structures and their angle relative to the droplet center. Some 246 rings were randomly positioned within droplets and 71 were positioned around the geometrical center of the droplets (317 droplets were analyzed, 35 independent experiments). When the distance between the ring center and the geometrical droplet center was larger than the ring radius (about 30% of the droplet radius), ring structures were counted to be asymmetric. (*C*) Fluorescent observations of F-actin organization in droplets having a diameter smaller than 20 µm (50 droplets, seven independent experiments). Sixty percent of the droplets failed in organizing a ring-like structure. Two main effects may influence F-actin organization at the scale of small droplets (<20 µm). First, the physical properties of both droplet boundary and filaments may directly constrain F-actin spatial organization. Indeed, some observations display a cortical organization of the filaments (*Left, Lower*). The high value of the extract/oil surface tension confers a rigid boundary to the droplet (10 mN/m). Therefore, when growing actin filaments encounter the extract-oil interface, normal compression forces are exerted, eventually causing filament buckling. This explains why when the droplet diameter reaches the characteristic F-actin persistence length (15 µm), filaments bend. This cortical organization may counteract inward F-actin flow. Second, the relatively small volumes of these droplets may limit the number of key components that control F-actin turnover. This lack of resources may eventually feedback on F-actin properties. (*D*) Kymographs of F-actin dynamics within droplets having a diameter smaller than 20 µm. (*E*) Observation of the dynamics of fluorescently labeled 2 µm-beads and F-actin meshwork. Scale bars = 10 µm.

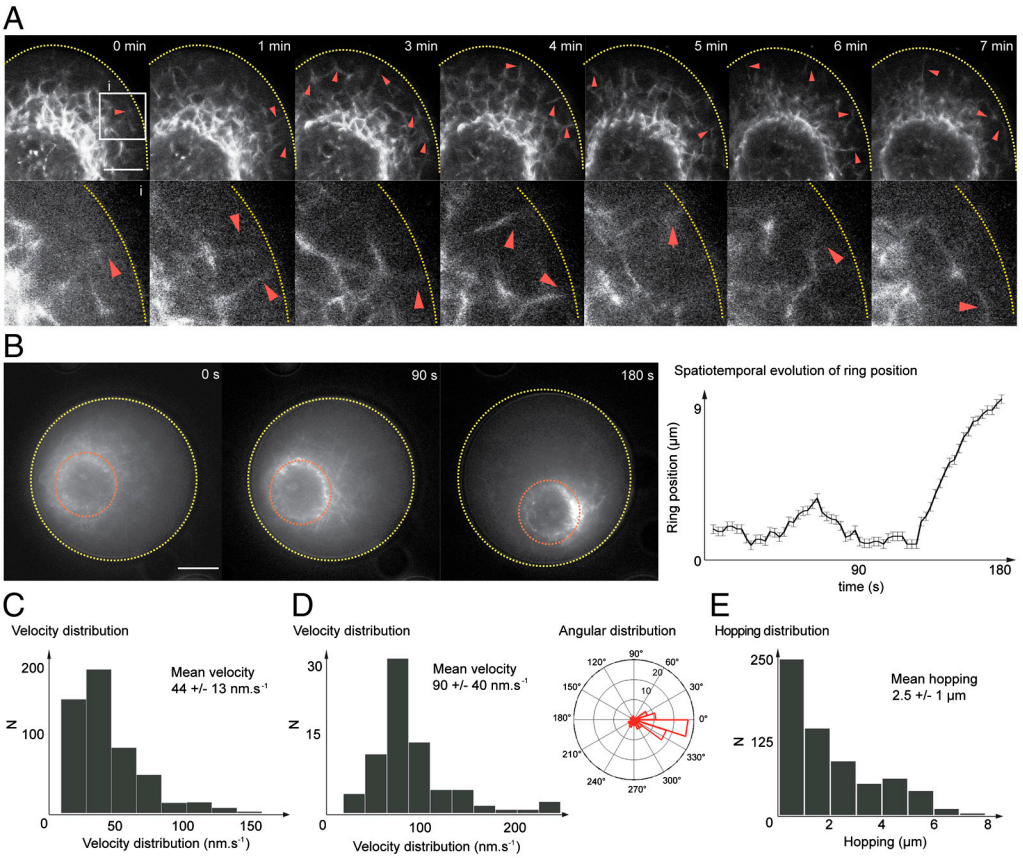

Fig. S2. (*A*) Time series of filament nucleation at the vicinity of the droplet boundary. Confocal observations. (*B*) Time-series acquisition showing dynamics of a ring-like structure within droplet. (*C*) Histogram of mean velocities in bulk extracts (N = 6 independent experiments, mean = 44 ± 13 nm s^{-1}, approximately 600 trajectories). (*D*) Velocity field distribution and angular orientation for single trajectories tracked within a single droplet. (*E*) Histogram of computed hopping distance (15 droplets analyzed). Scale bars = 10 µm.

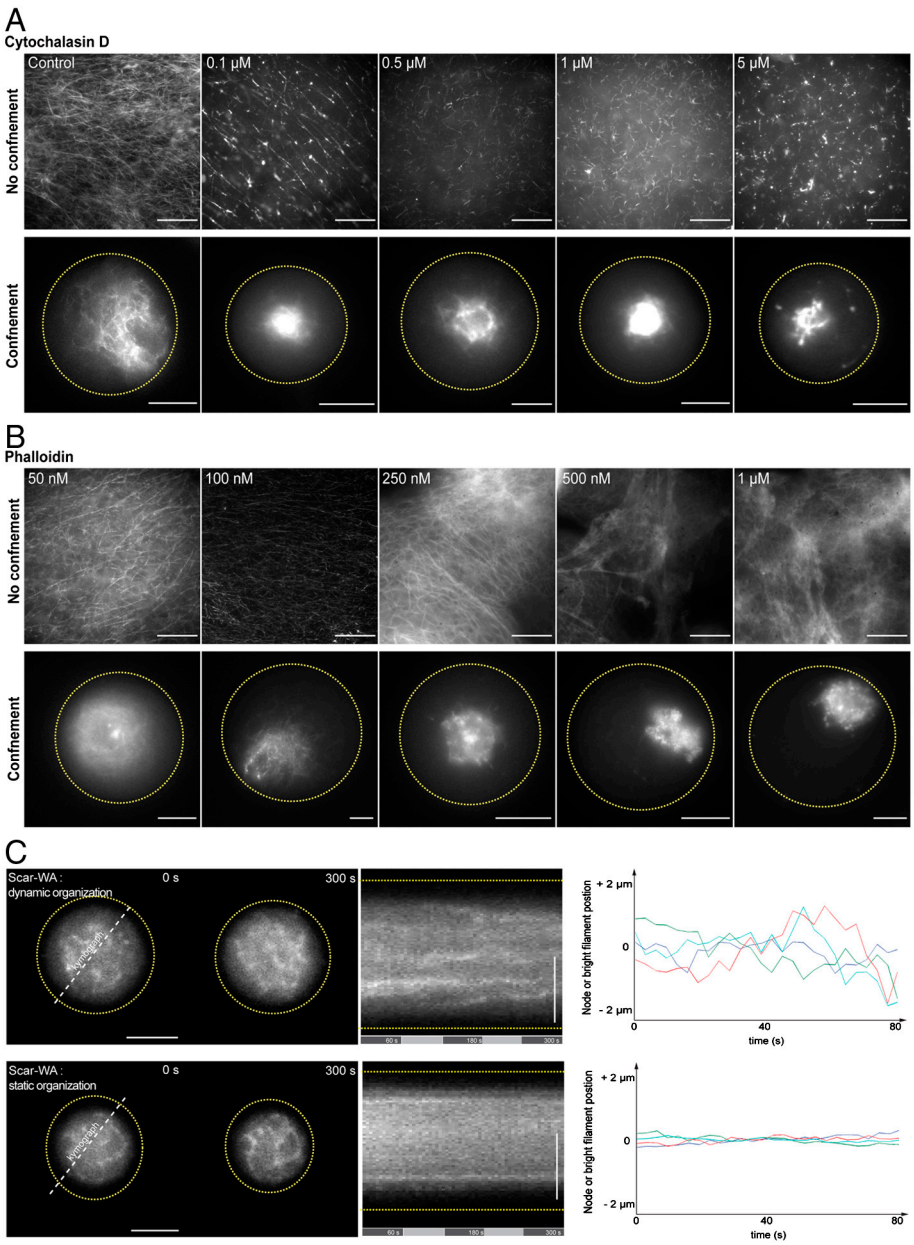

Fig. S3. Examples of F-actin network in unconfined environment (bulk) and within droplet for increasing concentration of cytochalasin D (*A*) and phalloidin (*B*), respectively. F-actin networks are not homogeneously distributed within droplets. Myosin motors that act as active cross-linkers may favor this spatial heterogeneity: Their contractile properties could promote filament clustering. (*C*) *Left*: Observation of F-actin meshwork in presence of Scar-WA/pWA. *Center*: Kymograph of F-actin time evolution for a dynamic and static organization respectively. *Right*: Tracking of four positions of the meshwork for a dynamic and static organization, respectively. Scale bars, 10 µm.

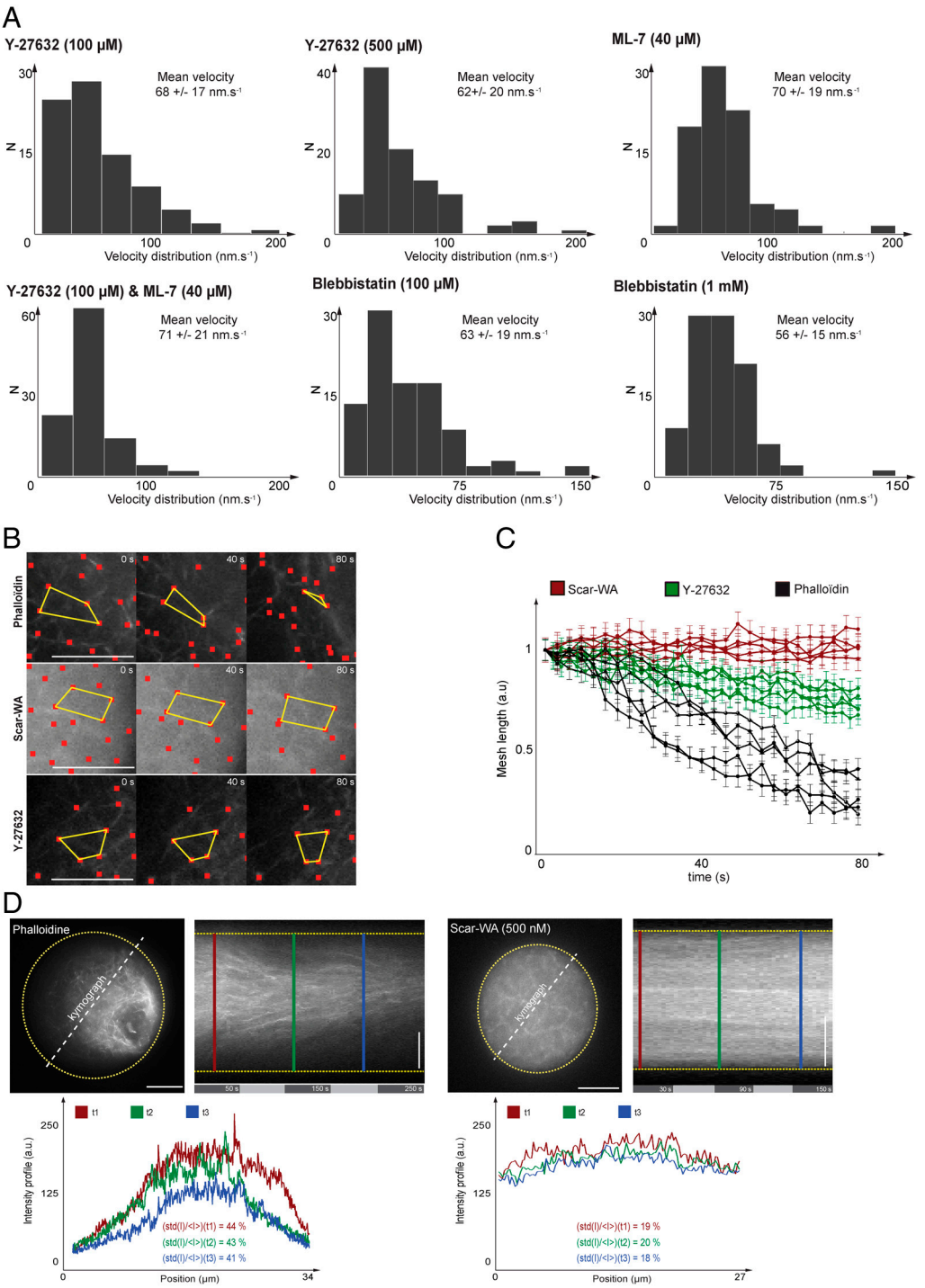

Fig. S4. (*A*) Velocity distribution computed for Y-27632, ML-7, and blebbistatin, respectively. ML-7 (40 µM, two independent experiments, 200 trajectories, five droplets). Y-27632 (100 µM, three independent experiments, 400 trajectories, 20 droplets). ML-7+Y-27632 (three independent experiments, 300 trajectories, 10 droplets). Blebbistatin 0.1 mM (two independent experiments, 200 trajectories, five droplets) and 1 mM (N = two experiments, 200 trajectories, five droplets). (*B*) Representative example of local reorganizations of F-actin network in unperturbed and perturbed extracts. (*C*) Evolution of mesh length as a function of time in unperturbed and perturbed extracts. (*D*) Measurements of the heterogeneity of the network in presence or absence of F-actin flow. The ratio between the standard deviation, std(I), and the mean value of the fluorescence intensity, ⟨I⟩, illustrates the concentration heterogeneity in presence or absence of F-actin flow. Scale bars, 10 µm.

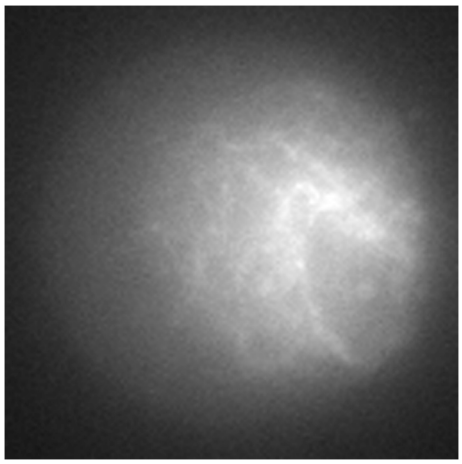

Movie S1. Example of F-actin network dynamics within a droplet. Time between two frames = 3 s. Time course = 186 s.

Movie S1 (AVI)

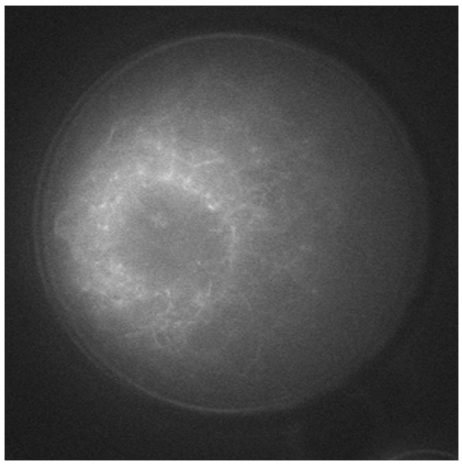

Movie S2. Example of F-actin network dynamics within a droplet. Time between two frames = 3 s. Time course = 183 s.

Movie S2 (AVI)

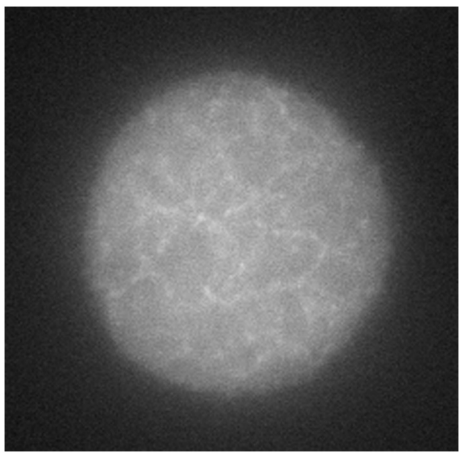

Movie S3. Effect of Scar-WA on F-actin network dynamics. Time between two frames = 3 s. Time course = 150 s.

Movie S3 (MOV)